Am J Physiol Cell Physiol 329: C646–C658, 2025.
First published July 22, 2025; doi:10.1152/ajpcell.00374.2025

american physiological society

AMERICAN JOURNAL OF PHYSIOLOGY
CELL PHYSIOLOGY

RESEARCH ARTICLE

Mechanisms Underlying Diversity in Cancer Cachexia

B0092 tumor-bearing mice are a new model for the study of cachexia in head and neck cancer

Patrick D. Livingston,[1] Ana Luiza Labbate Bonaldo,[1,7] Nicholas A. Jamnick,[1] Natalia M. Weinzierl,[1] Caleb J. Gammon,[1] Chandler S. Callaway,[1] Schuyler Lee,[2,5] Bifeng Gao,[2,5] Andrew Goodspeed,[4,5] Robson F. Carvalho,[7] Christian D. Young,[1] David J. Orlicky,[1] Douglas J. Adams,[3] Leah J. Novinger,[1,5] and Andrea Bonetto[1,5,6]

[1]*Department of Pathology, University of Colorado Anschutz Medical Campus, Aurora, Colorado, United States;* [2]*Department of Medicine-Pulmonary Sciences and Critical Care, University of Colorado Anschutz Medical Campus, Aurora, Colorado, United States;* [3]*Department of Orthopedics, University of Colorado Anschutz Medical Campus, Aurora, Colorado, United States;* [4]*Department of Biomedical Informatics, University of Colorado Anschutz Medical Campus, Aurora, Colorado, United States;* [5]*Cancer Center, University of Colorado Anschutz Medical Campus, Aurora, Colorado, United States;* [6]*Nutrition Obesity Research Center, University of Colorado Anschutz Medical Campus, Aurora, Colorado, United States; and* [7]*Department of Structural and Functional Biology, Institute of Biosciences, São Paulo State University (UNESP), Botucatu, São Paulo, Brazil*

Abstract

Head and neck cancer (HNC) accounts for ∼4% of all cancers but causes ∼15,000 deaths annually in the United States. Over 40% of HNC patients present with cachexia, a severe comorbidity associated with skeletal muscle defects, worsened treatment response, and poor outcomes. The mechanisms behind HNC cachexia remain unclear, partly due to limited small animal models. This study characterizes functional and molecular features of cachexia in a novel preclinical model using tobacco-induced B0092 oral squamous cell carcinoma in C57BL/6J mice. C2C12 myotubes were exposed to various concentrations of B0092 conditioned media (CM) to assess effects on myotube diameter and expression of muscle-specific ubiquitin ligases (MuRF-1 and atrogin-1). C57BL/6J male and female mice were implanted with B0092 cells (5×10^5 cells) to investigate musculoskeletal effects of HNC. RNA sequencing of muscle identified gene signatures associated with cachexia. Myotubes treated with B0092 CM showed atrophy already at 25% CM (−21%, $P < 0.01$), along with elevated MuRF-1 (+81%, $P < 0.05$) and atrogin-1 (+27%, $P < 0.05$). B0092 tumor growth in male mice led to muscle atrophy, reduced strength (−36%, $P < 0.001$), and lower bone mineral density (−8%, $P < 0.01$). Muscle atrophy correlated with increased MuRF-1 (+1.96-fold, $P < 0.05$) and atrogin-1 (+1.97-fold, $P < 0.05$). Female mice exhibited moderate cachexia despite similar tumor size. RNA sequencing of muscle in male B0092 hosts revealed mitochondrial dysfunction and upregulation of proteasome- and translation-related pathways, supporting a shift toward protein degradation and impaired energy metabolism. These findings suggest that B0092-bearing mice are valuable to uncover novel molecular pathways and potential therapeutic targets for HNC cachexia.

NEW & NOTEWORTHY This study introduces a novel preclinical model for head and neck cancer (HNC) cachexia using B0092 oral squamous cell carcinoma in C57BL/6J mice. Key findings include muscle atrophy, systemic musculoskeletal effects, and critical gene signatures associated with skeletal muscle wasting. These insights pave the way for potential therapeutic targets to mitigate cachexia in patients with HNC, offering a promising avenue for improving patient outcomes.

bone loss; cachexia; head and neck cancer; muscle wasting; muscle weakness

INTRODUCTION

Head and neck squamous cell carcinoma (HNSCC) is the seventh most common cancer type, accounting for ∼4% of all new cancer cases worldwide (1). Its incidence rate is predicted to swell an alarming 30% by 2030 (2, 3). Major risk factors for HNSCC include tobacco use, alcohol consumption, and human papillomavirus (HPV) infection. Although tobacco use and alcohol consumption still account for the largest population and the highest mortality rate of oral cancers (4), the incidence

Correspondence: A. Bonetto (andrea.bonetto@cuanschutz.edu).
Submitted 2 May 2025 / Revised 27 May 2025 / Accepted 15 July 2025

rate is declining. Conversely, HPV-induced oropharyngeal carcinomas (OPC), despite being attributed with better survivorship than consumption-induced oral cancers, has recently seen an increased incidence rate (5). Depending on their anatomical location, primary oral tumors are often the source of complications in patients, including dysarthria (difficulty speaking), dysphagia (difficulty eating), odynophagia (pain when swallowing), or dyspnea (difficulty breathing), all potentially leading to substantial weight loss and reduced quality of life (QoL) (6, 7). Interestingly, men are generally more susceptible to development of HNSCC than women (8), likely because of distinct lifestyle choices (e.g., smoking and drinking), hormonal differences, abnormal immune response, and higher risk of contracting HPV (9–12). Standard of care treatment for most kinds of HNC includes a combination of radiotherapy and chemotherapy (e.g., cisplatin and paclitaxel) (13), which have also been reported to contribute to the onset of musculoskeletal complications and worsened QoL, independent of cancer (14–16).

Of note, in addition to weight loss induced by swallowing complications, it is estimated that nearly half of all patients diagnosed with HNSCC present with cachexia (7, 17). Cachexia is described as a multifactorial wasting syndrome, whose onset frequently occurs in association with the later stages of various kinds of cancer (18). Symptoms are marked by loss of skeletal muscle mass, weight, and appetite, altogether leading to fatigue, poorer QoL, metabolic dysfunction, systemic inflammation, and overall increased morbidity and mortality (18–21). There are currently no approved therapies for cachexia, even though it is estimated to account for up to 30% of all cancer-related deaths (22). Muscle wasting as it pertains to cachexia is largely a result of an imbalance of protein homeostasis, and not simply malnutrition or lack of eating (23). Indeed, increased protein degradation through inflammation and overactivation of muscle-specific ubiquitin-ligases, alongside decreased protein synthesis, altogether result in diminished and weakened skeletal muscles (24, 25). A decrease in mitochondrial regulators and an overactivation of lipolysis are also hallmarks of this severe cancer comorbidity (19).

Cancer cachexia is a relatively understudied phenomenon in patients with HNC, who are already at high risk of malnutrition due to the location of the tumor and treatment-related toxicity (6, 26). This can be largely attributed to the lack of HNSCC preclinical animal models representative of the clinical scenario capable of forming tumors in immunocompetent mice and inducing cachexia, altogether impeding research progression and development of potential therapies. Although there have been various preclinical mouse models published for the study of HNSCC cachexia consequential to HPV infection and other less relevant sources (27–29), there is an alarming lack of literature characterizing the extent of cachexia caused by tobacco- or alcohol-induced HNSCC.

Taking this into account, the purpose of this study was to address the critical gap in preclinical modeling of cachexia in HNSCC tumors, particularly those induced by tobacco-related carcinogens. Indeed, despite the high prevalence of cachexia among patients with HNSCC and its significant contribution to morbidity and mortality, there remains a lack of robust, immunocompetent animal models that accurately reflect the clinical manifestations of this syndrome. This study aimed to establish and characterize a novel murine model of HNSCC-induced cachexia using the B0092 cell line, generated by exposing female C57BL/6J mice to 4-nitroquinoline 1-oxide (4NQO), a broadly studied tobacco mimetic carcinogen. Following the development of primary oral tumors and subsequent lung metastases, metastatic cells were isolated and reimplanted into syngeneic C57BL/6J mice to yield a stable and reproducible cell line derived from a HNSCC tumor, capable of forming tumors subcutaneously and inducing systemic cachexia-like symptoms, with limited interference from factors normally associated with clinical anorexia and influenced by tumor location, diet, and type of anticancer therapies. Overall, our investigations revealed that subcutaneously implanted B0092 tumors promote musculoskeletal abnormalities, likely consequential to high levels of tumor-derived proinflammatory factors and activation of signaling pathways associated with maintenance of skeletal muscle mass. By delineating the cachectic profile and identifying key proinflammatory and muscle-degenerative pathways activated in this model, we sought to lay the groundwork for the development of targeted therapeutic strategies to mitigate skeletal muscle loss and improve quality of life in patients with HNSCC.

METHODS

Cell Cultures

The B0092 cells were isolated from lung metastases in a C57BL/6J mouse implanted with the parental C57BL/6J syngeneic HNSCC line, namely the A1207, which was generated by inducing tongue SCC in a female C57BL/6J mouse with tobacco mimetic 4-nitroquinoline 1-oxide (4NQO), as previously described (30). The B0092 cells were grown in Dulbecco's modified Eagle's medium (DMEM)/F-12 supplemented with 10% fetal bovine serum (FBS) and 1% penicillin/streptomycin and maintained at 37°C in a humidified atmosphere with 5% CO_2. C2C12 myoblasts and 3T3-L1 fibroblasts (ATCC, Manassas, VA) were grown in high-glucose DMEM supplemented with 10% FBS and 1% penicillin/streptomycin. C2C12 differentiation was induced by switching 90% confluent myoblast cultures to DMEM containing 2% horse serum and 1% penicillin/streptomycin, replaced every other day for up to 5 days. B0092 and 3T3-L1 conditioned media (CM) were generated by adding fresh growth medium to ∼90% confluent cell layers, whereas C2C12 CM was obtained by supplementing fresh differentiation medium to 5-day differentiated myotube layers. After 48 h, the media were collected and centrifuged to remove any remaining debris. The CM was then immediately used or stored at −80°C. To determine the effects of tumor-derived mediators on fiber size and homeostasis, C2C12 myotubes were exposed to various concentrations (25%, 33%, and 50%) of B0092-derived CM for up to 48 h. Fresh (unconditioned) differentiation medium and equivalent concentrations of C2C12 CM were used as controls.

Animals

All in vivo experiments were approved by the Institutional Animal Care and Use Committee at University of Colorado Anschutz Medical Campus and were in compliance with the

National Institutes of Health Guidelines for Use and care of Laboratory Animals. In our initial experiment, to examine the procachexiogenic effects of the B0092 HNSCC cells, 10-wk-old C57BL/6J male mice (The Jackson Laboratory, Bar Harbor, ME) were randomized into two groups based off initial body mass and humanely euthanized when body weight loss was ∼10% of the initial body weight (IBW). The tumor hosts ($n = 6$; B0092) were injected subcutaneously with 5×10^5 B0092 cells in the intrascapular region, whereas the control mice ($n = 6$; control) were administered an isovolumetric (200 µL) subcutaneous injection of vehicle (sterile saline). In a second experiment aimed at investigating the effects of B0092 tumors in female hosts, 10-wk-old C57BL/6J female mice (The Jackson Laboratory, Bar Harbor, ME) were randomized into two groups as described earlier. The tumor hosts ($n = 5$; B0092) were injected subcutaneously with 5×10^5 B0092 cells in the intrascapular region, whereas the control animals ($n = 5$; control) were administered an equal volume of sterile saline. In both experiments, animal weights were monitored daily. Euthanasia entailed up to 1 mL of blood being drawn from intracardiac puncture followed by cervical dislocation. At the time of euthanasia (36 days for the male mice and 84 days for the female mice), skeletal muscles (gastrocnemius, quadriceps, and tibialis anterior) and other organs (heart, liver, spleen, epididymal fat, and kidneys) were harvested, weighed, and snap frozen, whereas the extensor digitorum longus (EDL) muscles were carefully isolated to undergo ex vivo muscle contractility measurement to determine the impact of B0092 tumors on muscle function. Tibialis anterior muscles were frozen in liquid nitrogen-cooled isopentane, then stored at −80°C and used for histological analysis.

EchoMRI

Body composition, including lean (muscle) and fat (adipose) tissue, was measured weekly throughout the study in unanesthetized mice. The mice were physically restrained using an EchoMRI whole body composition analyzer (EchoMRI LLC, Houston). Before scanning, a phantom containing vegetable oil was used to calibrate the fat component of the body composition measurements.

Assessment of Muscle Cross-Sectional Area

To assess skeletal muscle fiber cross-sectional area (CSA), 10-µm-thick cryosections taken at the midbelly of the tibialis anterior muscle were processed for hematoxylin-eosin (H&E) staining, as described previously (31, 32). H&E-stained sections were imaged using a Zeiss Axioscan 7, Germany. CSA was quantified in QuPath version 0.4.2 (33) using the Cellpose extension (34). For the analysis, 300–500 muscle fibers from four representative tibialis anterior samples per group were measured.

Assessment of Myotube Size

Five-day differentiated C2C12 myotubes were fixed in ice-cold acetone–methanol (50:50) at −20°C for 10 min, followed by incubation with an antimyosin heavy chain antibody (MF-20, 1:200; Developmental Studies Hybridoma Bank, Iowa City, IA) and an AlexaFluor 488-labelled secondary antibody (Invitrogen, Grand Island, NY). Analysis of myotube size was performed by measuring the average diameter of long, multinucleated fibers ($n = 250$–350 per condition), avoiding regions of clustered nuclei on a calibrated image using the ImageJ 1.53 software (35). Diameter was assessed only in mature myotubes possessing greater than three nuclei.

Cytokine Profiling Assay

Tumor secreted cytokines were assessed in B0092 CM (collected as described above) using a mouse cytokine/chemokine 32-plex discovery assay array (Eve Technologies, Calgary, AB, Canada). Tumor levels were compared to base DMEM/F-12 media as well as CM generated from 3T3-L1 fibroblasts. To ensure consistency across all experimental conditions and to eliminate physiological variability introduced by different serum lots, all media were supplemented with FBS from the same lot and prepared concurrently. This approach minimizes potential confounding effects on cytokine profiles in the conditioned media. Resulting data was graphed as raw pg/mL derived from comparison to a standard curve.

Real-Time Quantitative Polymerase Chain Reaction

RNA from quadriceps was isolated using the miRNeasy Mini kit (Qiagen, Valencia, CA) and following the protocol provided by the manufacturer. RNA was quantified by using a Nanodrop spectrophotometer (BioTek, Winooski, VT). Total RNA was reverse transcribed to cDNA by using the Verso cDNA kit (Thermo Fisher Scientific, Waltham, MA). Transcript levels were measured by real-time PCR (7500 Fast Real-Time PCR System: Applied Biosystems, Waltham Massachusetts) using the TaqMan gene expression assay system (Life Technologies, Carlsbad, CA). Expression levels for Atrogin-1 (Mm00499523_m1) and MuRF-1 (Mm01185221_m1) were assessed. Gene expression was normalized to TATA-binding protein (TBP) (Mm01277042_m1) levels using the standard $2^{-\Delta\Delta Ct}$ methods.

Bulk RNA Sequencing

Total RNA from skeletal muscle was extracted as described earlier. RNA purity, quantity, and integrity were determined with NanoDrop (Thermo Fisher Scientific, Waltham, MA) and TapeStation 4200 (Agilent, Santa Clara, CA) analysis before RNA sequencing (RNA-Seq) library preparation. The Universal Plus mRNA-Seq library preparation kit with NuQuant was used (Tecan, Männedorf, Switzerland) with an input of 200 ng of total RNA to generate RNA-Seq libraries. Paired-end sequencing reads of 150 bp were generated on NovaSeq 6000 (Illumina, San Diego, CA) sequencer at a target depth of 80 million paired-end reads per sample. Raw sequencing reads were demultiplexed using bcl2fastq. Raw data are available via the GEO gene expression omnibus, accession number GSE288471. RNA-Seq data were processed using the nf-core RNAseq pipeline (v. 3.12.0) (36). In brief, illumina adapters were removed using Cutadapt (v. 3.4) (37). Reads were aligned using STAR (2.7.9a) to the Ensembl mouse transcriptome (GRCm39 release 104) and quantified using Salmon (1.10.1) (38, 39). Raw data with counts by gene were generated using tximport on salmon quantified data (40). For downstream analysis, rlog normalization and differential expression analysis were performed using

DESeq2 (41). Principal component analysis (PCA) was conducted to assess sample variance. Differentially expressed genes (DEGs) between tumor-bearing and control samples were identified based on an adjusted P value < 0.05 and an absolute fold change ($|FC|$) > 1. The top 100 genes positively and negatively correlated with quadriceps muscle weight were selected for further analyses (Supplemental Table S1). To visualize the expression differences across groups, a heatmap was generated using Morpheus (42). Functional enrichment analysis of the 200 selected genes was performed using EnrichR (43–45). The two most highly associated genes from each pathway were depicted in an alluvial plot generated with SankeyMatic (https://sankeymatic.com/) and a heatmap created using Morpheus (42).

Ex Vivo Muscle Contractility

The contractile force in EDL muscles was measured through whole muscle contractility assessment. The EDL muscles were quickly dissected in a tray containing Tyrode solution (121 mM NaCl, 5.0 mM KCl, 1.8 mM $CaCl_2$, 0.5 mM $MgCl_2$, 0.4 mM NaH_2PO_4, 24 mM $NaHCO_3$, 0.1 mM EDTA, and 5.5 mM glucose), and stainless-steel hooks were tied to both tendons using 4-0 silk sutures. The muscles were then placed between a mounted force transducer (Aurora Scientific, Aurora, ON, Canada) and incubated in a stimulation heated bath containing Tyrode supplemented with continuous O_2/CO_2 (95/5%). Following a 10-min incubation period, the maximum twitch force was obtained by determining optimal muscle length (L0). Force data were collected and analyzed with the Dynamic Muscle Control/Data Acquisition and Dynamic Muscle Control Data Analysis programs (Aurora Scientific), and EDL muscle weight and L0 were used to determine specific force.

Dual-Energy X-Ray Absorptiometry

Bone mineral density (BMD) and bone mineral content (BMC) were assessed by means of dual-energy X-ray absorptiometry (DXA) scanning of formalin-fixed femurs. As per manufacturer's guidelines, to calibrate and validate the apparatus, a phantom was scanned using the InAnalyzer system (MediKors, Jungwon-gu, Seongnam-si, Gyeonggi-do, Republic of Korea) before scanning the first bone. Regions of interest were defined around the whole bone to gain the BMD from each individual femur.

Analysis of Bone Microstructure

After euthanasia, the right femur was dissected from each mouse, fixed for 2 days in 10% neutral-buffered formalin, and transferred into 70% ethanol. Trabecular and cortical bone morphometry were quantified at the distal metaphysis and middiaphysis, respectively, using X-ray micro-computed tomography (μCT50, Scanco Medical AG, Bassersdorf, Switzerland). Femurs were imaged in 70% ethanol at 70 kVp (200 μA) within a 20-mm diameter field of view, collecting 2,000 conebeam projections per revolution at an integration time of 500 msec. Three-dimensional images were reconstructed at 10 μm resolution using standard convolution back projection algorithms with Shepp and Logan filtering and rendered at a discrete voxel density of 1,000,000 voxels/mm^3 (isometric 10 μm voxels). Bone mineral was calibrated to a discrete-step hydroxyapatite phantom and segmented from marrow and soft tissue in conjunction with a constrained Gaussian filter to reduce noise, applying mineral density thresholds of 550 and 700 mg HA/cm^3 for trabecular and cortical bone, respectively. Volumetric regions for trabecular bone analysis were selected within the endosteal borders to include the secondary spongiosa of femoral metaphyses located ~1 mm (~7% of length) from the growth plate and extending 5% of femur length proximally. Trabecular morphometric parameters were measured without imposing a presumed structural model to obtain direct measures of trabecular volume fraction (BV/TV), thickness (Tb.Th), number (Tb.N), spacing (Tb.Sp), connectivity density (Conn.D), and tissue mineral density (Tiss.D).

Statistics

All statistical analyses were performed using GraphPad Prism 9.0.0 (GraphPad Software, San Diego, CA). Two-tailed Student's t tests were performed to determine significant differences between control and tumor-bearing animals. One-way ANOVA tests were used to determine significance of factor secreted into conditioned media. Statistical significance was set at $P \leq 0.05$, and the data were presented as means ± standard deviation.

RESULTS

B0092 HNSCC Cells Induce Atrophy in C2C12 Myotubes

To evaluate the effects of HNSCC tumor-derived factors on skeletal muscle, we exposed 5-day-differentiated, mature C2C12 myotubes to various concentrations of B0092 CM (25%, 33%, and 50%). Fresh medium and equivalent concentrations of C2C12 CM were used as respective controls. After 48 h of treatment, C2C12 CM had no significant effect on myotube diameter, whereas B0092 CM consistently induced myotube atrophy at all concentrations tested (25% CM: −21%, $P < 0.01$; 33% CM: −29%, $P < 0.01$; 50% CM: −24%, $P < 0.05$ vs. C2C12 CM; Fig. 1, *A* and *B*). To shed light on the mechanisms associated with B0092-dependent muscle atrophy, we investigated the expression of the muscle-specific ubiquitin ligases MuRF-1 and atrogin-1, which are commonly upregulated in conditions associated with skeletal muscle atrophy (46, 47). Both ligases were significantly elevated in B0092 CM-treated myotubes across all dilutions, with MuRF-1 showing a more pronounced response, indicating activation of a hypercatabolic program (Fig. 1, *C* and *D*). Interestingly, we also observed modest but significant increases in MuRF-1 and atrogin-1 expression in the 50% C2C12 CM group versus fresh medium, suggesting that nutrient depletion may contribute to catabolic signaling under high CM concentrations. However, expression levels remained consistently higher in the B0092 CM groups compared with their C2C12 CM counterparts, reinforcing the role of tumor-derived factors in driving the cachectic phenotype.

B0092 Cancer Cells Secrete High Levels of Proinflammatory Mediators

To better understand whether HNSCC is a source of immune and proinflammatory mediators that could induce wasting in C2C12 myotubes, we performed cytokine multiplex

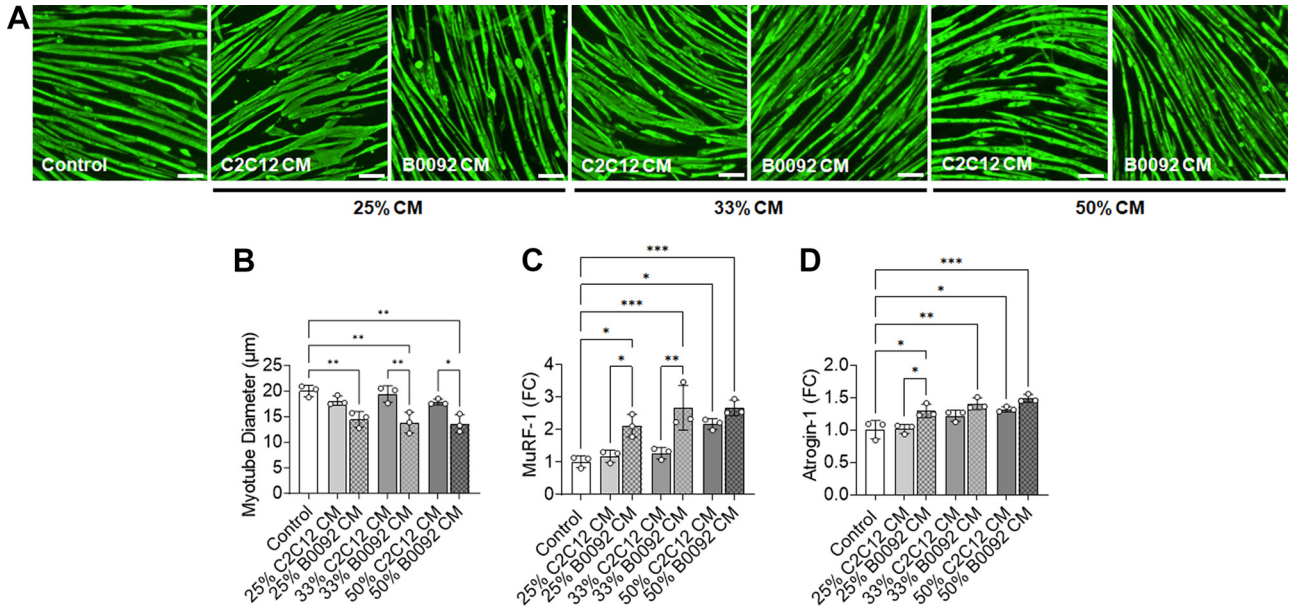

Figure 1. B0092 cells induce myotube atrophy. *A*: representative images of C2C12 myotubes exposed to 25%, 33%, and 50% B0092 conditioned medium (CM) for up to 48 h. Fresh differentiation medium and equivalent amounts of C2C12 CM were used as controls. *B*: myotube diameter (expressed in μm) was measured in long, multinucleated fibers ($n = 250–350$ per condition) avoiding regions of clustered nuclei. Data are representative of 3 technical replicates ($n = 3$ per experimental group). Scale bar: 100 μm. Assessment of MuRF-1 (*C*) and atrogin-1 (*D*) muscle-specific E3 ubiquitin ligase RNA expression in myotubes exposed to 25%, 33%, and 50% CM for 2 h assessed by qPCR. TATA-binding protein (TBP) was used as housekeeping gene for normalization. Data expressed as means ± SD. Significant differences: $^{*}P < 0.05$; $^{**}P < 0.01$; $^{***}P < 0.001$.

profiling of B0092 CM. As shown in Fig. 2, *A–G*, when compared with unconditioned DMEM/F12K medium and CM generated from 3T3-L1 fibroblasts, the B0092 cells were generally found to secrete higher levels of soluble factors previously implicated in the onset of cachexia, including IL-6 (8.55 pg/mL) and LIF (50 pg/mL). Other factors were also markedly elevated, including macropahge colony-stimulating factor (M-CSF) (0.45 pg/mL), granulocyte colony-stimulating factor (G-CSF) (630 pg/mL), keratinocyte-derived cytokine (KC) (4,785 pg/mL), LIX (248 pg/mL), and VEGFA (614 pg/mL). Thereby, these observations suggested that the B0092 HNC tumors have the potential to promote skeletal muscle atrophy due to elevations in tumor-derived proinflammatory factors.

B0092 Tumor Hosts Experience Loss of Whole Body, Lean, and Fat Mass

To examine whether growth of the B0092 tumors contributed to the development of cachexia in vivo, 10-wk-old male C57BL/6J mice were subcutaneously injected in the scapular region with 5×10^5 B0092 cells (control: $n = 6$; B0092: $n = 6$). Both tumor-bearing hosts and control animals were assessed for body weight and compositional changes over the duration of the entire experiment. After an initial lag phase, at approximately *day 33* body weight in the B0092 hosts showed a significant deviation from the control animals (−14%, $P < 0.01$; data not shown). At the time of euthanasia (*day 36*), B0092 tumors were excised and weighed, reaching ~3% of the mouse body mass (~0.8 g on average; Fig. 3*A*). Initial histologic characterization of H&E-stained tumors revealed large areas supported by fibrous collagen (Supplemental Fig. S1*A*) and necrotic areas exhibiting fractured nuclei (Supplemental Fig. S1*B*). Picro-Sirius Red staining also uncovered the presence of strands of fibrillar collagen between sheets and cords of large epithelioid cancer cells (Supplemental Fig. S1*C*) and larger bundles of collagen along with smaller bundles and even

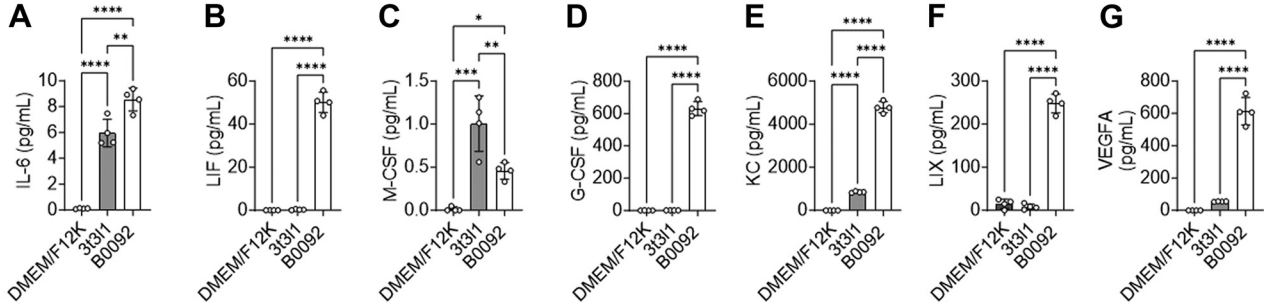

Figure 2. B0092 conditioned medium (CM) shows elevations in proinflammatory/procachectic cytokines. Concentrations (expressed in pg/mL) of representative proinflammatory cytokines in (unconditioned) base media, 3T3-L1 fibroblast CM, and B0092 CM ($n = 4$) assessed via multiplex cytokine profiling. Levels of IL-6 (*A*), LIF (*B*), M-CSF (*C*), G-CSF (*D*), KC (*E*), LIX (*F*), VEGFA (*G*). Data expressed as means ± SD. Significant differences: $^{*}P < 0.05$; $^{**}P < 0.01$; $^{***}P < 0.001$; $^{****}P < 0.0001$.

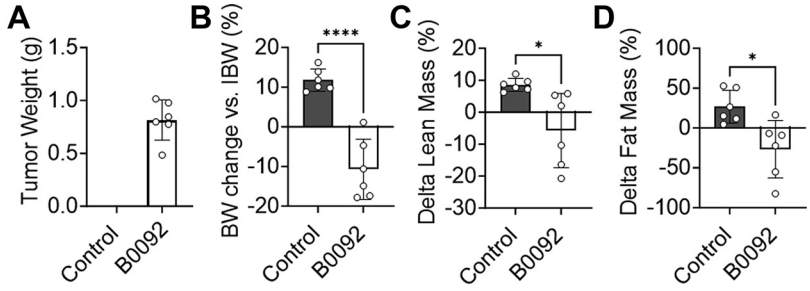

Figure 3. B0092 tumors induce loss of body mass and body composition. *A*: tumor weight (expressed in grams) in control and B0092 hosts ($n = 6$). *B*: change in body mass percentage compared with initial body weight (IBW) in control and B0092-bearing mice. Changes in lean muscle mass (*C*) (control: +8.6% vs. B0092: −5.7%, $P < 0.0001$) and fat mass (*D*) (control: +26% vs. B0092: −26%, $P < 0.05$) assessed by EchoMRI with respect to *day 0* values. Data expressed as means ± SD. Significant differences: *$P <$ 0.05; ****$P < 0.0001$.

single fibrils (Supplemental Fig. S1*D*), although no clearly definable overall pattern was observed. Lipid deposition was also present, although it appeared unrelated to the pattern of collagen fibrils. Similar to models of HPV-derived HNC cachexia (27), at end point, the B0092 tumor-bearing mice had lost ∼11% of their initial body weight, whereas respective controls had gained ∼11% their initial body weight ($P < 0.01$; Fig. 3*B*). Loss of whole body mass in the B0092 hosts also aligned with progressive changes in lean (control: +8.6% vs. B0092: −5.7%, $P < 0.0001$) and fat mass (control: +26% vs. B0092: −26%, $P < 0.05$; Fig. 3*C*) compared with the control animals.

Consistent with the significant body weight loss, skeletal muscle was severely diminished in tumor-bearing mice, as marked by reduced gastrocnemius (−19%, $P < 0.05$%; Fig. 4*A*), quadriceps (−30%, $P < 0.01$; Fig. 4*B*), and tibialis anterior (−25%, $P < 0.01$; Fig. 4*C*) weights. Alongside the depletion of skeletal muscle mass, muscle functional impairments were also observed, as described in previously characterized cachexia models. (48) In particular, ex vivo functional testing of the extensor digitorum longus (EDL) revealed significant muscle weakness in the B0092 hosts compared with the controls (−36%, $P < 0.0001$; Fig. 4*D*), also consistent with reduced fiber size in the tibialis anterior muscle at time of euthanasia (−37%, $P < 0.01$; Fig. 4, *E* and *F*). In agreement with our in vitro data, the skeletal muscle of B0092 hosts also displayed marked upregulations of muscle-specific E3 ubiquitin ligase mRNA expression (MuRF-1: +65%, $P < 0.05$; atrogin-1: +79%, $P < 0.05$) versus control (Fig. 4, *G* and *H*). Accompanying the skeletal muscle atrophy, severe cardiac wasting (−34%, $P < 0.01$; Fig. 4*I*) and diminished gonadal fat (−72%, $P < 0.001$; Fig. 4*J*), liver (−28%, $P < 0.0001$; Fig. 4*K*), and kidney (−24%, $P < 0.0001$; Fig. 4*L*) masses were also observed in the B0092 tumor hosts. Notably, unlike other murine models for the study of cancer cachexia, the spleen size was unchanged compared with the control mice (data not shown).

Given that men are two to three times more likely to develop head and neck cancers compared with women, we aimed to determine whether the present model could also

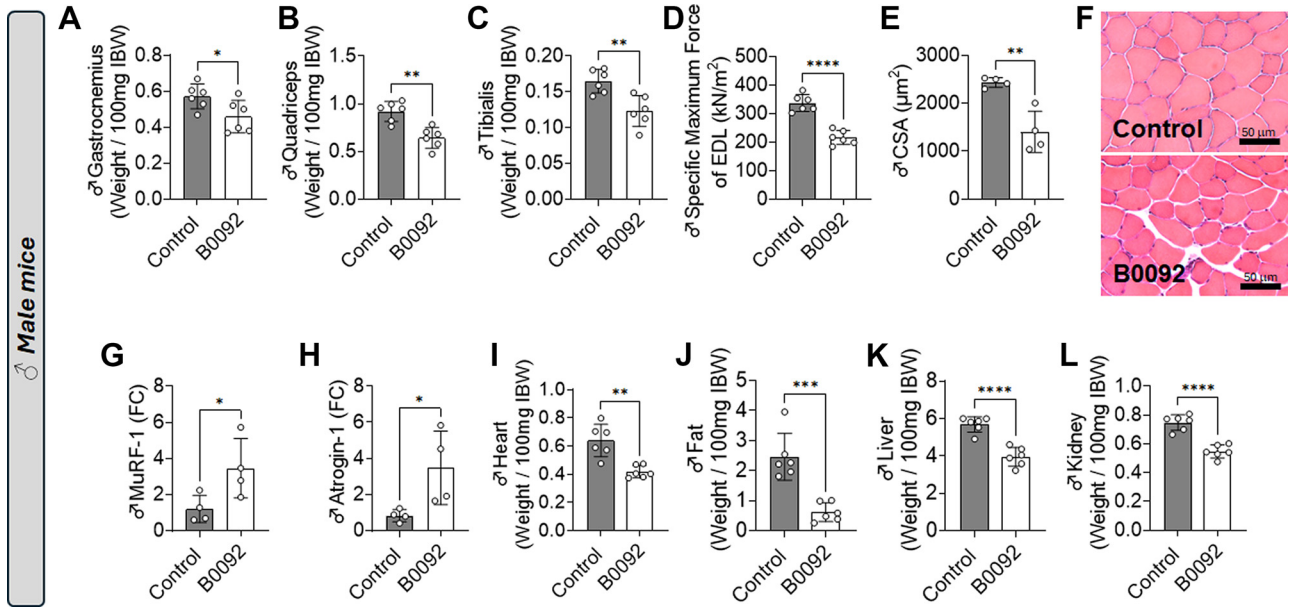

Figure 4. Skeletal muscle size and function are perturbed by B0092 tumors in male tumor hosts. Gastrocnemius (*A*), tibialis anterior (*B*), and quadriceps weights (*C*) [normalized to initial body weight (IBW)] in control and B0092-bearing male animals ($n = 6$). *D*: extensor digitorum longus (EDL) ex vivo-specific force (measured at 150 Hz and expressed as kN/m^2; $n = 6$). *E*: quantification of cross-sectional areas (CSA) in tibialis anterior muscles from control and B0092 hosts ($n = 4$). *F*: representative images from hematoxylin-eosin (H&E)-stained cross sections of tibialis anterior muscle collected at time of euthanasia in control and B0092 hosts. qPCR quantification of MuRF-1 (*G*) and atrogin-1 (*H*) gene expression in the quadriceps muscle of control and B0092-bearing mice ($n = 4$). Heart (*I*), gonadal fat (*J*), liver (*K*), and kidney (*L*) weights (normalized to IBW) from control and B0092 hosts ($n = 6$). Data expressed as means ± SD. Data were normalized to TBP. Data expressed as means ± SD. Significant differences: *$P < 0.05$; **$P < 0.01$; ***$P < 0.001$; ****$P < 0.0001$.

replicate these sex-specific differences in cachexia progression. Epidemiological data also suggest that men have a higher incidence and severity of cancer-associated cachexia (49). To this end, age-matched female C57BL/6J mice (control: $n = 5$; B0092: $n = 4$) were injected with the same number of B0092 cells used in the male cohort. Similar to males, the female mice exhibited an initial lag phase in tumor growth but reached end point criteria much later (84 days after inoculation). Interestingly, despite developing slightly larger tumors compared with the male mice (~1.18 g; data not shown), the female mice showed only modest body weight loss (~3.5% of the IBW; Fig. 5*A*) and not significant reductions in muscle mass (Fig. 5, *B* and *C*). Notably, these animals did not reach the typical 10% body weight loss threshold used for cachexia classification and were euthanized once tumors reached sizes comparable with those in the male study (Fig. 4). Nonetheless, functional impairments were evident, with the EDL muscles from tumor-bearing females showing moderately decreased muscle strength (−13%, $P < 0.01$ vs. control; Fig. 5*D*). In addition, organ weight loss followed a similar pattern to that observed in males, with modest but significant reductions in heart (−20%, $P < 0.01$), liver (−16%, $P < 0.05$), kidney (−14%, $P < 0.05$), and adipose tissue (−72%, $P < 0.05$) compared with controls (Fig. 5, *E*–*H*).

Tumor Hosts Show Decreased Trabecular Bone Parameters Alongside Increased Bone Resorption

To determine whether bone mass was affected by the presence of B0092 tumors, we assessed bone mineral content (BMC) and bone mineral density (BMD) in formalin-fixed femurs by using DXA, in line with our previous findings (50). Although BMC was unchanged in controls (Fig. 6*A*), BMD was significantly decreased in the bones from B0092 hosts (−8%, $P < 0.001$; Fig. 6*B*). To further investigate bone architecture, we then performed micro-computed tomography (micro-CT) analysis of femurs at the time of euthanasia. Cortical bone volume was unaffected (data not shown), but several parameters indicated trabecular bone loss in tumor-bearing animals. Although no significant changes were observed in trabecular bone volume fraction (BV/TV; −11%, not significant; Fig. 6*C*), decreases were seen in trabecular number (Tb.N; −12%, $P < 0.01$; Fig. 6*D*) and trabecular connectivity (Conn.D; −33%, $P < 0.05$; Fig. 6*E*), also in line with increased trabecular spacing (Tb.Sp; +12%, $P < 0.05$ Fig. 6*F*). Tissue mineral density (Tiss.D) was unaffected by B0092 tumors (Fig. 6*G*). These findings, supported by the 3-D renderings (Fig. 6*H*), indicate a diminished trabecular bone phenotype in B0092-bearing mice. To explore the mechanism underlying this bone loss, we quantified osteoclast activity of tartrate-resistant acid phosphatase (TRAP)-stained femur longitudinal sections (Fig. 6*I*). B0092-bearing mice exhibited a significant increase in TRAP-positive osteoclasts (+75%, $P < 0.001$; Fig. 6*J*), thereby suggesting that bone loss in the B0092 hosts is likely a consequence of increased bone resorption.

Bulk RNA-Seq of Quadriceps Reveals Pathways of Interest

To elucidate the molecular mechanisms driving skeletal muscle wasting in the B0092 model of cancer cachexia, we performed a comprehensive transcriptomic analysis using total RNA extracted from quadriceps muscles of control and B0092-bearing mice using bulk RNA sequencing. Principal component analysis (PCA) revealed a clear separation between the two groups, with PC1 accounting for most of the variance (Fig. 7*A*), indicating a distinct transcriptional profile in tumor-bearing animals. Analysis of the top 50 differentially expressed genes (DEGs) revealed greater variability among upregulated genes, whereas downregulated genes exhibited a more consistent pattern across samples (Fig. 7*B*). Notably, genes responsible for maintaining elements of mitochondrial homeostasis were significantly downregulated in the quadriceps of B0092 tumor-bearing animals. These included key regulators of mitochondrial fusion (e.g., *Opa1* and *Mfn2*) and components of the electron transport chain (e.g., *Atp5a*), suggesting impaired mitochondrial function (Fig. 7*C*). This trend was reflected in the overall DEG distribution, with more genes downregulated (736) than upregulated (420) in tumor-bearing muscle (Fig. 7*D*). To investigate the relationship between the DEGs and muscle atrophy, we correlated transcript levels with final quadriceps muscle weights. The top 100 positively and

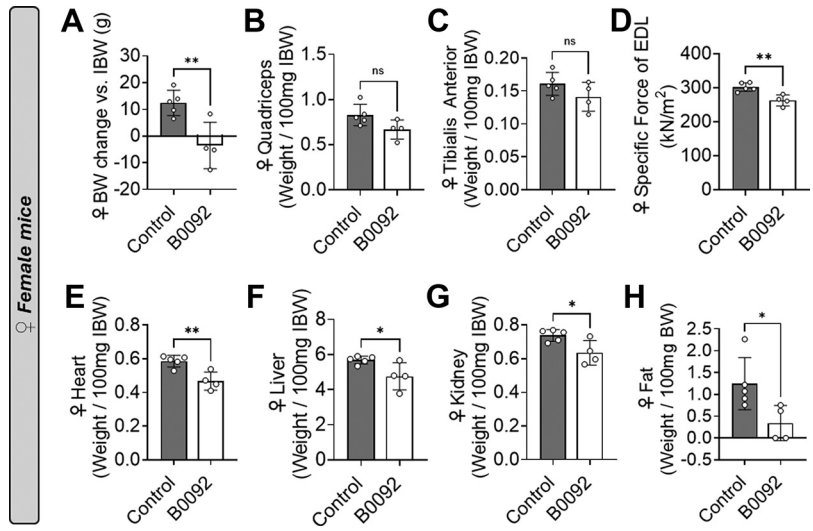

Figure 5. B0092 tumors implanted in female mice exhibit a modest cachectic response. *A*: change in body mass compared with initial body weight (IBW) in control and B0092-bearing female mice ($n = 5$). Quadriceps (*B*) and tibialis anterior (*C*) weights (normalized to IBW) in control and B0092-bearing animals ($n = 5$). *D*: extensor digitorum longus (EDL) ex vivo-specific force (measured at 150 Hz and expressed as kN/m^2) in control and B0092-bearing female mice ($n = 4$ or 5). Heart (*E*), liver (*F*), kidney (*G*), and gonadal fat (*H*) weights (normalized to IBW) from control and B0092 hosts ($n = 6$). Data expressed as means ± SD. ns, not significant. Significant differences: $^*P < 0.05$; $^{**}P < 0.01$.

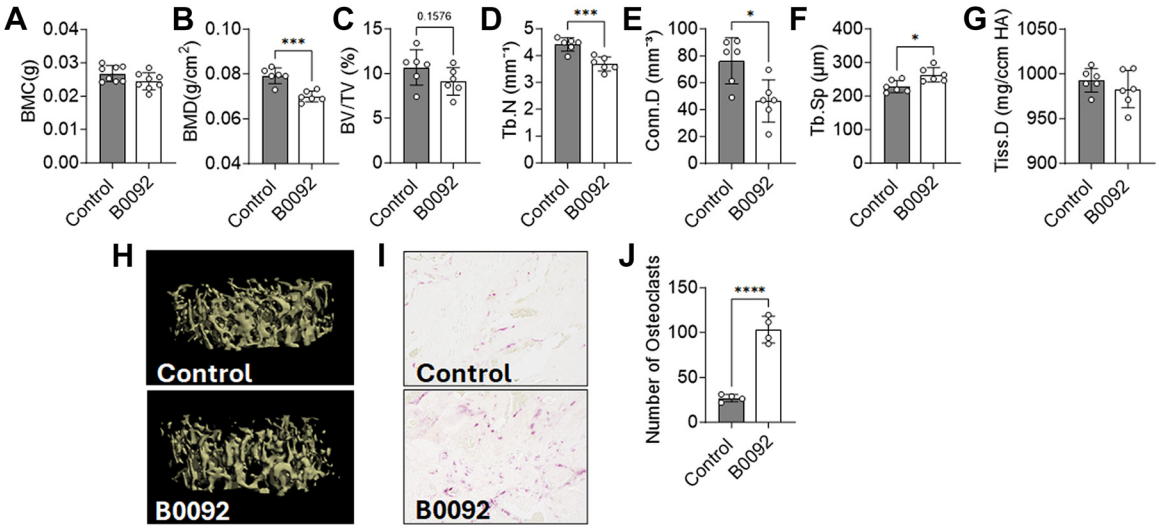

Figure 6. B0092 tumors induce trabecular bone loss. *A*: bone mineral content (*A*) (BMC; expressed as grams) and bone mineral density (*B*) (BMD; expressed as g/cm^2) were assessed via dual-energy X-ray absorptiometry (DXA) ($n = 6$). Trabecular bone volume (BV/TV; expressed as %) (*C*), trabecular number (Tb.N; expressed in mm^{-1}) (*D*), connectivity density (Conn.D; expressed in mm^{-3}) (*E*), trabecular spacing (Tb.Sp; expressed in mm) (*F*), and tissue mineral density (*G*) (Tiss.D; expressed in mg/ccm HA) in control and B0092-bearing animals ($n = 6$). *H*: representative three-dimensional (3-D) rendering of trabecular bone in control and B0092 hosts. Representative images of tartrate-resistant acid phosphatase (TRAP)-stained longitudinal femur sections from controls and B0092 bearers (*I*) and quantification (expressed as number of osteoclasts; $n = 4$) (*J*). Data expressed as means ± SD. Significant differences: $^*P < 0.05$; $^{***}P < 0.001$; $^{****}P < 0.0001$.

negatively correlated genes were then visualized on a heatmap (Fig. 7*E*). Genes positively correlated with muscle weight (e.g., *LTO1*, *Gm5069*, and *Kif26b*; Supplemental Table S1) were downregulated in B0092-bearing mice, whereas negatively correlated genes (e.g., *Mrps26*, *Gstm2*, and *Rpl6l*; Supplemental Table S1) were upregulated. To better understand the functional relevance of the differentially correlated genes, we performed an enrichment analysis (Fig. 6*F*). Downregulation of genes associated with pathways critical for muscle integrity, such as actin cytoskeleton organization (*Acta1*), mitochondrial function (*Timm22*), and extracellular collagen formation (*Egfl7*), was positively correlated with the loss of quadriceps weight. Conversely, several of the top upregulated genes associated with muscle loss, including *Usp15* and *Nod2*, are known to be involved in pathways related to proteasome function and NF-κB signaling (Fig. 7*F*), therefore suggesting potential activation of these catabolic processes in the quadriceps of tumor-bearing mice. Altogether, these findings further substantiate the extensive molecular remodeling underlying muscle degeneration in the B0092 model, characterized by suppressed mitochondrial and structural maintenance pathways and activation of proteolytic and inflammatory signaling. This molecular signature not only aligns with known cachexia mechanisms but also identifies potential avenues for therapeutic intervention.

DISCUSSION

In this study, we established and characterized a novel immunocompetent murine model of tobacco-related head and neck squamous cell carcinoma (HNSCC)-induced cachexia, using the B0092 cell line. This line was derived from C57BL/6J mice exposed to 4NQO, a well-established tobacco mimetic carcinogen, to mimic tobacco-induced HNSCC. The resulting model faithfully reproduces hallmark features of cancer cachexia, including progressive skeletal muscle atrophy, loss of adipose and organ mass, and impaired muscle function. These phenotypes are consistent with those observed in other well-established models of cachexia, such as pancreatic, ovarian, and colorectal cancer (50–52), thereby validating the utility of our mouse model for studying cachexia in the context of HNSCC. Importantly, this model addresses a critical gap in the field: the lack of preclinical systems that especially reflect the cachexia-inducing potential of tobacco-associated HNSCC. Indeed, although HPV-driven models have been previously studied, tobacco-related HNSCC remains clinically prevalent and is associated with higher mortality (53, 54), thus warranting for more exhaustive investigations in this area.

Our in vivo and in vitro analyses revealed hallmark features of cachexia, including increased expression of muscle-specific E3 ubiquitin ligases (MuRF-1 and atrogin-1), altogether suggestive of a hypercatabolic state. These findings were also supported by transcriptomic data showing downregulation of mitochondrial and oxidative phosphorylation pathways and upregulation of catabolic and inflammatory signaling. These molecular signatures are consistent with those reported in other models of cancer cachexia (46, 55) and are also in line with observations generated in models of cachexia induced by HPV-derived HNSCC (27, 56, 57), thus further reinforcing the robustness of our system.

Interestingly, we observed high levels of IL-6 and LIF in the conditioned media of B0092 cancer cells. These proinflammatory cytokines are well-established mediators of cancer cachexia and are also strongly associated with activation of an acute-phase response and skeletal muscle wasting (55, 58, 59). In addition to IL-6 and LIF, we also detected increased levels of other tumor-derived factors, including KC (CXCL1) and VEGFA. Although KC was previously

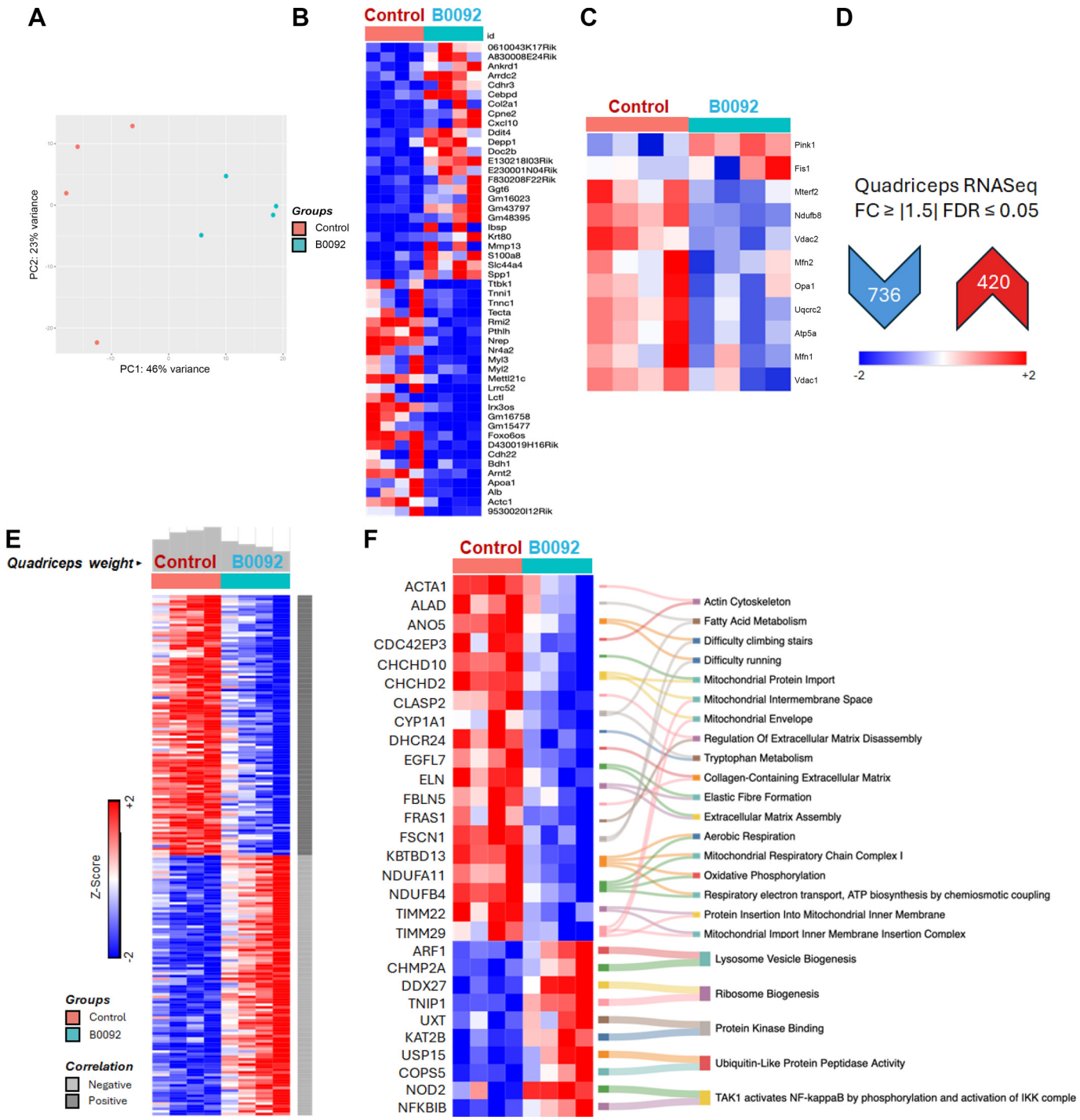

Figure 7. RNA sequencing reveals differentially expressed genes and pathways in skeletal muscle undergoing atrophy as a result of B0092 tumor growth. *A*: principal component analysis (PCA) of control (red) and B0092 [head and neck cancer (HNC); light blue] samples ($n = 4$), with the majority of variance being acounted for by PC1. *B*: top 50 dysregulated genes in B0092-bearing mice (25 upregulated and 25 downregulated). *C*: DEGs with a role in mitochondrial homeostasis in muscle of B0092-bearing mice. *D*: fold change and FDR cutoff describing differential expression, total number of upregulated and downregulated genes, and color scale for heatmap. *E*: heatmap illustrating top 200 dysregulated genes correlated with quadriceps weights (100 upregulated and 100 downregulated) associated with significantly enriched pathways and ontologies ($P \leq 0.05$, minimum of 2 genes per pathway). *F*: alluvial plot mapping the connections between genes and the respective enriched pathways and ontologies.

implicated in cachexia through its role in modulating inflammation and immune responses in both tumor and microenvironment (60, 61), the contribution of VEGFA to muscle wasting remains less defined. Notably, here we observed a paradoxical downregulation of VEGFA expression in skeletal muscle, despite its high secretion by the tumor. This suggests a potential disconnect between tumor-derived and tissue-specific VEGFA signaling. Interestingly, VEGFA has previously been shown to enhance skeletal muscle regeneration by promoting vascular perfusion and directly interacting

with myocytes (62, 63). Moreover, in *Drosophila*, the VEGFA ortholog Pvf1 was shown to contribute to tissue wasting through activation of MEK in skeletal muscle and adipose tissue (64). Together, our observations point to a novel regulatory mechanism worth exploring in future studies.

Notably, in our study, we also identified dysregulation of mitochondrial dynamics in skeletal muscle. Indeed, our transcriptomics data revealed reduced expression of mitochondrial fusion markers (MFN-2 and OPA-1), alongside a decline in mitochondria seen through diminished VDAC expression (58), thereby suggesting impaired mitochondrial homeostasis—a process not previously reported in HNSCC cachexia models. Given the role of mitochondrial dysfunction in driving hypercatabolism and muscle wasting (65), this finding may offer new insights into the metabolic underpinnings of cachexia and potential therapeutic targets.

In the present model, we also observed moderate trabecular bone loss in tumor-bearing mice, accompanied by increased osteoclast activity. This suggests that abnormal bone muscle cross talk may contribute to cachexia in HNSCC. Although we did not directly assess for the presence of tumor dissemination in the bones of B0092 hosts, nonetheless our previous findings support the idea that defective bone muscle communication involving various signaling pathways and circulating factors that can mutually affect both bone and muscle tissues (66–69) may play a significant role in the development and progression of cachexia, even in the absence of bone metastases. Although bone loss in HNSCC is often attributed to radiation therapy in clinical settings, particularly in the vertebrae and cervical spine (70, 71), our findings indicate that tumor-induced bone resorption may occur independently. Future studies should explore whether bone-targeted therapies (e.g., bisphosphonates and denosumab) combined with traditional therapies for HNC may be beneficial in preserving skeletal muscle mass through regulation of bone resorption (72).

In this study, we did not perform direct statistical comparisons between male and female animals, as the two experiments were conducted independently. Nonetheless, sex-specific differences in cachexia progression were also evident, with female mice exhibiting delayed onset and reduced severity of muscle wasting compared with males and despite comparable tumor burden. These observations are consistent with previous reports, indicating that male tumor hosts are more susceptible to cachexia and tend to experience more severe muscle loss and worsened outcomes compared with females (49). Given that the B0092 cells were derived from immunocompetent female hosts, it is plausible that the female hosts exhibited slower tumor progression due to a more compatible (or less reactive) immune environment (73, 74). Although our functional and molecular analyses were primarily conducted in male mice, thereby reflecting the higher prevalence of HNC in the male population, this model also provides a biologically relevant platform for investigating cachexia mechanisms in female hosts, an underrepresented group in preclinical HNSCC research.

Despite the novelty of these findings, we acknowledge several limitations in our approach. First, the use of subcutaneous rather than orthotopic implantation limits insights into tumor-microenvironment interactions. Indeed, although the growth of orthotopic tumors could provide more insights into the role of the tumor microenvironment, the present approach allowed us to focus exclusively on the direct systemic effects consequential to HNSCC growth, thus also minimizing interference from factors normally associated with anorexia or dysphagia. Second, we did not assess the metastatic potential of B0092 tumors, despite their origin from lung metastases. Considering that the B0092 cell line is derived from lung metastases, future studies will need to evaluate whether primary B0092 tumors can spontaneously metastasize to distal organ or tissues, thus potentially contributing to a higher degree of cachexia. Finally, we did not compare the B0092 model with other HPV^+ HNSCC cell lines. Therefore, we cannot speculate on whether the molecular mechanisms driving cachexia in the presence of B0092 tumors are HPV-independent.

Conclusions

In summary, the B0092 model provides a robust, reproducible, and biologically relevant platform for studying tobacco-related HNSCC-induced cachexia. It faithfully recapitulates key features of cancer cachexia, including muscle wasting, metabolic dysfunction, and systemic inflammation while also introducing novel aspects such as mitochondrial dysregulation and bone-muscle cross talk, which have not been previously described in HNSCC models. Its alignment with established cachexia mechanisms, combined with its unique context and observed sex-specific dynamics, makes this model a valuable tool for advancing our understanding of cancer-associated muscle wasting and for identifying and testing therapeutic interventions aimed at preserving muscle mass and function in affected patients.

DATA AVAILABILITY

Raw RNA-sequencing data are available via the GEO gene expression omnibus, accession number GSE288471. The data underlying this article will be shared on reasonable request to the corresponding author.

SUPPLEMENTAL MATERIAL

Supplemental Fig. S1: https://doi.org/10.6084/m9.figshare.29534033.

Supplemental Table S1: https://doi.org/10.6084/m9.figshare.29534294.

ACKNOWLEDGMENTS

Graphical abstract created with a licensed version of BioRender.com.

GRANTS

This study was supported by the Department of Pathology and the Cancer Center at the University of Colorado Anschutz Medical Campus, and by grants from American Cancer Society (132013-RSG-18-010-01-CCG), NIH/NIAMS (R01AR079379 and R01AR080051), NIH/NCI (CO HNC SPORE Grant P50CA261605 via a Developmental Research Project), and the Cancer League of Colorado (AWD-242527-AB) to A.B. C.S.C. and N.A.J. were supported by T32 Institutional Training Grants from NIH/NIAMS and NIH/NCI (T32AR080630 and T32CA190216). The Energy

Balance Assessment Core at CU NORC, which allowed the use of their DEXA and EchoMRI systems, was partly supported by NIH/NIDDK (P30DK048520). The Genomics and the Bioinformatics and Biostatistics Shared Resources at CU Anschutz were partly supported by NIH/NCI (P30CA046934), by the Alpine HPC system, which is jointly funded by the University of Colorado Boulder, the University of Colorado Anschutz, Colorado State University, and by the National Science Foundation (Award No. 2201538).

DISCLOSURES

No conflicts of interest, financial or otherwise, are declared by the authors.

AUTHOR CONTRIBUTIONS

P.D.L., C.D.Y., L.J.N., and A.B. conceived and designed research; P.D.L., N.A.J., N.M.W., C.J.G., C.S.C., and D.J.A. performed experiments; P.D.L., A.L.L.B., N.A.J., S.L., B.G., A.G., R.F.C., D.J.O., D.J.A., L.J.N., and A.B. analyzed data; P.D.L., A.L.L.B., S.L., B.G., A.G., R.F.C., D.J.O., L.J.N., and A.B. interpreted results of experiments; P.D.L., A.G., and A.B. prepared figures; P.D.L. and A.L.L.B. drafted manuscript; P.D.L., R.F.C., C.D.Y., D.J.O., D.J.A., L.J.N., and A.B. edited and revised manuscript; P.D.L., A.L.L.B., N.A.J., N.M.W., C.J.G., C.S.C., S.L., B.G., A.G., R.F.C., C.D.Y., D.J.O., D.J.A., L.J.N., and A.B. approved final version of manuscript.

REFERENCES

1. **Siegel RL**, **Kratzer TB**, **Giaquinto AN**, **Sung H**, **Jemal A.** Cancer statistics, 2025. *CA Cancer J Clin* 75: 10–45, 2025. doi:10.3322/caac.21871.
2. **Bray F**, **Ferlay J**, **Soerjomataram I**, **Siegel RL**, **Torre LA**, **Jemal A.** Global cancer statistics 2018: GLOBOCAN estimates of incidence and mortality worldwide for 36 cancers in 185 countries. *CA Cancer J Clin* 68: 394–424, 2018 [Erratum in *CA Cancer J Clin* 70: 313, 2020]. doi:10.3322/caac.21492.
3. **Ferlay J**, **Colombet M**, **Soerjomataram I**, **Mathers C**, **Parkin DM**, **Piñeros M**, **Znaor A**, **Bray F.** Estimating the global cancer incidence and mortality in 2018: GLOBOCAN sources and methods. *Int J Cancer* 144: 1941–1953, 2019. doi:10.1002/ijc.31937.
4. **Goyal N**, **Day A**, **Epstein J**, **Goodman J**, **Graboyes E**, **Jalisi S**, **Kiess AP**, **Ku JA**, **Miller MC**, **Panwar A**, **Patel VA**, **Sacco A**, **Sandulache V**, **Williams AM**, **Deschler D**, **Farwell DG**, **Nathan CA**, **Fakhry C**, **Agrawal N.** Head and neck cancer survivorship consensus statement from the American Head and Neck Society. *Laryngoscope Investig Otolaryngol* 7: 70–92, 2022. doi:10.1002/lio2.702.
5. **Chaturvedi AK**, **Engels EA**, **Pfeiffer RM**, **Hernandez BY**, **Xiao W**, **Kim E**, **Jiang B**, **Goodman MT**, **Sibug-Saber M**, **Cozen W**, **Liu L**, **Lynch CF**, **Wentzensen N**, **Jordan RC**, **Altekruse S**, **Anderson WF**, **Rosenberg PS**, **Gillison ML.** Human papillomavirus and rising oropharyngeal cancer incidence in the United States. *J Clin Oncol* 29: 4294–4301, 2011. doi:10.1200/JCO.2011.36.4596.
6. **Johnson DE**, **Burtness B**, **Leemans CR**, **Lui VWY**, **Bauman JE**, **Grandis JR.** Head and neck squamous cell carcinoma. *Nat Rev Dis Primers* 6: 92, 2020 [Erratum in *Nat Rev Dis Primers* 9: 4, 2023]. doi:10.1038/s41572-020-00224-3.
7. **Jager-Wittenaar H**, **Dijkstra PU**, **Dijkstra G**, **Bijzet J**, **Langendijk JA**, **van der Laan B**, **Roodenburg JLN.** High prevalence of cachexia in newly diagnosed head and neck cancer patients: an exploratory study. *Nutrition* 35: 114–118, 2017. doi:10.1016/j.nut.2016.11.008.
8. **Park JO**, **Nam IC**, **Kim CS**, **Park SJ**, **Lee DH**, **Kim HB**, **Han KD**, **Joo YH.** Sex differences in the prevalence of head and neck cancers: a 10-year follow-up study of 10 million healthy people. *Cancers (Basel)* 14: 2521, 2022. doi:10.3390/cancers14102521.
9. **Lewin F**, **Norell SE**, **Johansson H**, **Gustavsson P**, **Wennerberg J**, **Biörklund A**, **Rutqvist LE.** Smoking tobacco, oral snuff, and alcohol in the etiology of squamous cell carcinoma of the head and neck: a population-based case-referent study in Sweden. *Cancer* 82: 1367–1375, 1998. doi:10.1002/(SICI)1097-0142(19980401)82:7<1367::AID-CNCR21>3.0.CO;2-3.
10. **Franceschi S**, **Bidoli E**, **Negri E**, **Barbone F**, **La Vecchia C.** Alcohol and cancers of the upper aerodigestive tract in men and women. *Cancer Epidemiol Biomarkers Prev* 3: 299–304, 1994.
11. **Hashibe M**, **Brennan P**, **Benhamou S**, **Castellsague X**, **Chen C**, **Curado MP**, **et al.** Alcohol drinking in never users of tobacco, cigarette smoking in never drinkers, and the risk of head and neck cancer: pooled analysis in the International Head and Neck Cancer Epidemiology Consortium. *J Natl Cancer Inst* 99: 777–789, 2007 [Erratum in *J Natl Cancer Inst* 100: 225, 2008]. doi:10.1093/jnci/djk179.
12. **Anantharaman D**, **Marron M**, **Lagiou P**, **Samoli E**, **Ahrens W**, **Pohlabeln H**, **Slamova A**, **Schejbalova M**, **Merletti F**, **Richiardi L**, **Kjaerheim K**, **Castellsague X**, **Agudo A**, **Talamini R**, **Barzan L**, **Macfarlane TV**, **Tickle M**, **Simonato L**, **Canova C**, **Conway DI**, **McKinney PA**, **Thomson P**, **Znaor A**, **Healy CM**, **McCartan BE**, **Hashibe M**, **Brennan P**, **Macfarlane GJ.** Population attributable risk of tobacco and alcohol for upper aerodigestive tract cancer. *Oral Oncol* 47: 725–731, 2011. doi:10.1016/j.oraloncology.2011.05.004.
13. **Machiels JP**, **René Leemans C**, **Golusinski W**, **Grau C**, **Licitra L**, **Gregoire V**; **EHNS Executive Board.** Squamous cell carcinoma of the oral cavity, larynx, oropharynx and hypopharynx: EHNS-ESMO-ESTRO Clinical Practice Guidelines for diagnosis, treatment and follow-up. *Ann Oncol* 31: 1462–1475, 2020. doi:10.1016/j.annonc.2020.07.011.
14. **Conte E**, **Bresciani E**, **Rizzi L**, **Cappellari O**, **De Luca A**, **Torsello A**, **Liantonio A.** Cisplatin-induced skeletal muscle dysfunction: mechanisms and counteracting therapeutic strategies. *Int J Mol Sci* 21: 1242, 2020. doi:10.3390/ijms21041242.
15. **Grossberg AJ**, **Chamchod S**, **Fuller CD**, **Mohamed AS**, **Heukelom J**, **Eichelberger H**, **Kantor ME**, **Hutcheson KA**, **Gunn GB**, **Garden AS**, **Frank S**, **Phan J**, **Beadle B**, **Skinner HD**, **Morrison WH**, **Rosenthal DI.** Association of body composition with survival and locoregional control of radiotherapy-treated head and neck squamous cell carcinoma. *JAMA Oncol* 2: 782–789, 2016. doi:10.1001/jamaoncol.2015.6339.
16. **Grossberg AJ**, **Mohamed AS**, **Fuller CD.** Cachexia in radiotherapy-treated patients with head and neck cancer-reply. *JAMA Oncol* 2: 831–832, 2016. doi:10.1001/jamaoncol.2016.1458.
17. **Baracos VE**, **Martin L**, **Korc M**, **Guttridge DC**, **Fearon KCH.** Cancer-associated cachexia. *Nat Rev Dis Primers* 4: 17105, 2018. doi:10.1038/nrdp.2017.105.
18. **Fearon KC**, **Glass DJ**, **Guttridge DC.** Cancer cachexia: mediators, signaling, and metabolic pathways. *Cell Metab* 16: 153–166, 2012. doi:10.1016/j.cmet.2012.06.011.
19. **Pin F**, **Barreto R**, **Couch ME**, **Bonetto A**, **O'Connell TM.** Cachexia induced by cancer and chemotherapy yield distinct perturbations to energy metabolism. *J Cachexia Sarcopenia Muscle* 10: 140–154, 2019. doi:10.1002/jcsm.12360.
20. **Roeland EJ**, **Bohlke K**, **Baracos VE**, **Bruera E**, **Del Fabbro E**, **Dixon S**, **Fallon M**, **Herrstedt J**, **Lau H**, **Platek M**, **Rugo HS**, **Schnipper HH**, **Smith TJ**, **Tan W**, **Loprinzi CL.** Management of cancer cachexia: ASCO guideline. *J Clin Oncol* 38: 2438–2453, 2020. doi:10.1200/JCO.20.00611.
21. **Huot JR**, **Livingston PD**, **Pin F**, **Thomas CR**, **Jamnick NA**, **Callaway CS**, **Bonetto A.** Long-term musculoskeletal consequences of chemotherapy in pediatric mice. *Function (Oxf)* 5: zqae011, 2024. doi:10.1093/function/zqae011.
22. **Han J**, **Harrison L**, **Patzelt L**, **Wu M**, **Junker D**, **Herzig S**, **Berriel Diaz M**, **Karampinos DC.** Imaging modalities for diagnosis and monitoring of cancer cachexia. *EJNMMI Res* 11: 94, 2021. doi:10.1186/s13550-021-00834-2.
23. **Khan B**, **Gand LV**, **Amrute-Nayak M**, **Nayak A.** Emerging mechanisms of skeletal muscle homeostasis and cachexia: the SUMO perspective. *Cells* 12: 644, 2023. doi:10.3390/cells12040644.
24. **Acharyya S**, **Ladner KJ**, **Nelsen LL**, **Damrauer J**, **Reiser PJ**, **Swoap S**, **Guttridge DC.** Cancer cachexia is regulated by selective targeting of skeletal muscle gene products. *J Clin Invest* 114: 370–378, 2004. doi:10.1172/JCI20174.
25. **Zimmers TA**, **Fishel ML**, **Bonetto A.** STAT3 in the systemic inflammation of cancer cachexia. *Semin Cell Dev Biol* 54: 28–41, 2016. doi:10.1016/j.semcdb.2016.02.009.
26. **Villa A**, **Sonis S.** Toxicities associated with head and neck cancer treatment and oncology-related clinical trials. *Curr Probl Cancer* 40: 244–257, 2016. doi:10.1016/j.currproblcancer.2016.06.001.

27. **Olson B**, **Norgard MA**, **Levasseur PR**, **Zhu X**, **Marks DL.** Physiologic and molecular characterization of a novel murine model of metastatic head and neck cancer cachexia. *J Cachexia Sarcopenia Muscle* 12: 1312–1332, 2021. doi:10.1002/jcsm.12745.
28. **Cannon T**, **Couch M**, **Yin X**, **Guttridge D**, **Lai V**, **Shores C.** Comparison of animal models for head and neck cancer cachexia. *Laryngoscope* 117: 2152–2158, 2007. doi:10.1097/MLG.0b013e3181453658.
29. **Lai KC**, **Hong ZX**, **Hsieh JG**, **Lee HJ**, **Yang MH**, **Hsieh CH**, **Yang CH**, **Chen YR.** IFIT2-depleted metastatic oral squamous cell carcinoma cells induce muscle atrophy and cancer cachexia in mice. *J Cachexia Sarcopenia Muscle* 13: 1314–1328, 2022. doi:10.1002/jcsm.12943.
30. **Nguyen KA**, **DePledge LN**, **Bian L**, **Ke Y**, **Samedi V**, **Berning AA**, **Owens P**, **Wang XJ**, **Young CD.** Polymorphonuclear myeloid-derived suppressor cells and phosphatidylinositol-3 kinase gamma are critical to tobacco-mimicking oral carcinogenesis in mice. *J Immunother Cancer* 11: e007110, 2023. doi:10.1136/jitc-2023-007110.
31. **Huot JR**, **Pin F**, **Narasimhan A**, **Novinger LJ**, **Keith AS**, **Zimmers TA**, **Willis MS**, **Bonetto A.** ACVR2B antagonism as a countermeasure to multi-organ perturbations in metastatic colorectal cancer cachexia. *J Cachexia Sarcopenia Muscle* 11: 1779–1798, 2020. doi:10.1002/jcsm.12642.
32. **Bonetto A**, **Andersson DC**, **Waning DL.** Assessment of muscle mass and strength in mice. *Bonekey Rep* 4: 732, 2015. doi:10.1038/bonekey.2015.101.
33. **Bankhead P**, **Loughrey MB**, **Fernández JA**, **Dombrowski Y**, **McArt DG**, **Dunne PD**, **McQuaid S**, **Gray RT**, **Murray LJ**, **Coleman HG**, **James JA**, **Salto-Tellez M**, **Hamilton PW.** QuPath: open source software for digital pathology image analysis. *Sci Rep* 7: 16878, 2017. doi:10.1038/s41598-017-17204-5.
34. **Stringer C**, **Wang T**, **Michaelos M**, **Pachitariu M.** Cellpose: a generalist algorithm for cellular segmentation. *Nat Methods* 18: 100–106, 2021. doi:10.1038/s41592-020-01018-x.
35. **Schneider CA**, **Rasband WS**, **Eliceiri KW.** NIH Image to ImageJ: 25 years of image analysis. *Nat Methods* 9: 671–675, 2012. doi:10.1038/nmeth.2089.
36. **Ewels PA**, **Peltzer A**, **Fillinger S**, **Patel H**, **Alneberg J**, **Wilm A**, **Garcia MU**, **Di Tommaso P**, **Nahnsen S.** The nf-core framework for community-curated bioinformatics pipelines. *Nat Biotechnol* 38: 276–278, 2020. doi:10.1038/s41587-020-0439-x.
37. **Martin M.** Cutadapt removes adapter sequences from high-throughput sequencing reads. *EMBnet J* 17: 10–12, 2011. doi:10.14806/ej.17.1.200.
38. **Dobin A**, **Davis CA**, **Schlesinger F**, **Drenkow J**, **Zaleski C**, **Jha S**, **Batut P**, **Chaisson M**, **Gingeras TR.** STAR: ultrafast universal RNA-seq aligner. *Bioinformatics* 29: 15–21, 2013. doi:10.1093/bioinformatics/bts635.
39. **Patro R**, **Duggal G**, **Love MI**, **Irizarry RA**, **Kingsford C.** Salmon provides fast and bias-aware quantification of transcript expression. *Nat Methods* 14: 417–419, 2017. doi:10.1038/nmeth.4197.
40. **Soneson C**, **Love MI**, **Robinson MD.** Differential analyses for RNA-seq: transcript-level estimates improve gene-level inferences. *F1000Res* 4: 1521, 2015. doi:10.12688/f1000research.7563.2.
41. **Love MI**, **Huber W**, **Anders S.** Moderated estimation of fold change and dispersion for RNA-seq data with DESeq2. *Genome Biol* 15: 550, 2014. doi:10.1186/s13059-014-0550-8.
42. **Starruß J**, **de Back W**, **Brusch L**, **Deutsch A.** Morpheus: a user-friendly modeling environment for multiscale and multicellular systems biology. *Bioinformatics* 30: 1331–1332, 2014. doi:10.1093/bioinformatics/btt772.
43. **Kuleshov MV**, **Jones MR**, **Rouillard AD**, **Fernandez NF**, **Duan Q**, **Wang Z**, **Koplev S**, **Jenkins SL**, **Jagodnik KM**, **Lachmann A**, **McDermott MG**, **Monteiro CD**, **Gundersen GW**, **Ma'ayan A.** Enrichr: a comprehensive gene set enrichment analysis web server 2016 update. *Nucleic Acids Res* 44: W90–97, 2016. doi:10.1093/nar/gkw377.
44. **Chen EY**, **Tan CM**, **Kou Y**, **Duan Q**, **Wang Z**, **Meirelles GV**, **Clark NR**, **Ma'ayan A.** Enrichr: interactive and collaborative HTML5 gene list enrichment analysis tool. *BMC Bioinformatics* 14: 128, 2013. doi:10.1186/1471-2105-14-128.
45. **Xie Z**, **Bailey A**, **Kuleshov MV**, **Clarke DJB**, **Evangelista JE**, **Jenkins SL**, **Lachmann A**, **Wojciechowicz ML**, **Kropiwnicki E**, **Jagodnik KM**, **Jeon M**, **Ma'ayan A.** Gene set knowledge discovery with Enrichr. *Curr Protoc* 1: e90, 2021. doi:10.1002/cpz1.90.
46. **Mota R**, **Rodríguez JE**, **Bonetto A**, **O'Connell TM**, **Asher SA**, **Parry TL**, **Lockyer P**, **McCudden CR**, **Couch ME**, **Willis MS.** Post-translationally modified muscle-specific ubiquitin ligases as circulating biomarkers in experimental cancer cachexia. *Am J Cancer Res* 7: 1948–1958, 2017.
47. **Costelli P**, **Muscaritoli M**, **Bossola M**, **Penna F**, **Reffo P**, **Bonetto A**, **Busquets S**, **Bonelli G**, **Lopez-Soriano FJ**, **Doglietto GB**, **Argilés JM**, **Baccino FM**, **Fanelli FR.** IGF-1 is downregulated in experimental cancer cachexia. *Am J Physiol Regul Integr Comp Physiol* 291: R674–R683, 2006. doi:10.1152/ajpregu.00104.2006.
48. **Huot JR**, **Pin F**, **Bonetto A.** Muscle weakness caused by cancer and chemotherapy is associated with loss of motor unit connectivity. *Am J Cancer Res* 11: 2990–3001, 2021 [Erratum in *Am J Cancer Res* 12: 1435, 2022].
49. **Zhong X**, **Zimmers TA.** Sex differences in cancer cachexia. *Curr Osteoporos Rep* 18: 646–654, 2020. doi:10.1007/s11914-020-00628-w.
50. **Pin F**, **Barreto R**, **Kitase Y**, **Mitra S**, **Erne CE**, **Novinger LJ**, **Zimmers TA**, **Couch ME**, **Bonewald LF**, **Bonetto A.** Growth of ovarian cancer xenografts causes loss of muscle and bone mass: a new model for the study of cancer cachexia. *J Cachexia Sarcopenia Muscle* 9: 685–700, 2018. doi:10.1002/jcsm.12311.
51. **Bonetto A**, **Rupert JE**, **Barreto R**, **Zimmers TA.** The colon-26 carcinoma tumor-bearing mouse as a model for the study of cancer cachexia. *J Vis Exp* 117: 54893, 2016. doi:10.3791/54893.
52. **Ducharme JB**, **Carelock ME**, **Schonk MM**, **Al-Zaeed NM**, **Zhang W**, **Judge SM**, **Judge AR.** Identification of a senescence-associated transcriptional program in skeletal muscle of cachectic pancreatic-tumor-bearing mice. *Am J Physiol Cell Physiol* 328: C1125–C1134, 2025. doi:10.1152/ajpcell.00816.2024.
53. **Hashibe M**, **Brennan P**, **Chuang SC**, **Boccia S**, **Castellsague X**, **Chen C**, **et al.** Interaction between tobacco and alcohol use and the risk of head and neck cancer: pooled analysis in the International Head and Neck Cancer Epidemiology Consortium. *Cancer Epidemiol Biomarkers Prev* 18: 541–550, 2009. doi:10.1158/1055-9965.EPI-08-0347.
54. **Barsouk A**, **Aluru JS**, **Rawla P**, **Saginala K**, **Barsouk A.** Epidemiology, risk factors, and prevention of head and neck squamous cell carcinoma. *Med Sci (Basel)* 11: 42, 2023. doi:10.3390/medsci11020042.
55. **Bonetto A**, **Aydogdu T**, **Kunzevitzky N**, **Guttridge DC**, **Khuri S**, **Koniaris LG**, **Zimmers TA.** STAT3 activation in skeletal muscle links muscle wasting and the acute phase response in cancer cachexia. *PLoS One* 6: e22538, 2011. doi:10.1371/journal.pone.0022538.
56. **Cannon T**, **Shores C**, **Yin X**, **Dahlman J**, **Guttridge D**, **Lai V**, **George J**, **Buzkova P**, **Couch M.** Immunocompetent murine model of cancer cachexia for head and neck squamous cell carcinoma. *Head Neck* 30: 320–326, 2008. doi:10.1002/hed.20698.
57. **Sasaki A**, **Takeda D**, **Kawai H**, **Tadokoro Y**, **Murakami A**, **Yatagai N**, **Arimoto S**, **Nagatsuka H**, **Akashi M**, **Hasegawa T.** Transcutaneous carbon dioxide suppresses skeletal muscle atrophy in a mouse model of oral squamous cell carcinoma. *PLoS One* 19: e0302194, 2024. doi:10.1371/journal.pone.0302194.
58. **Huot JR**, **Novinger LJ**, **Pin F**, **Bonetto A.** HCT116 colorectal liver metastases exacerbate muscle wasting in a mouse model for the study of colorectal cancer cachexia. *Dis Model Mech* 13: dmm043166, 2020. doi:10.1242/dmm.043166.
59. **Seto DN**, **Kandarian SC**, **Jackman RW.** A key role for leukemia inhibitory factor in C26 cancer cachexia. *J Biol Chem* 290: 19976–19986, 2015. doi:10.1074/jbc.M115.638411.
60. **Jiang Y**, **Tsoi LC**, **Billi AC**, **Ward NL**, **Harms PW**, **Zeng C**, **Maverakis E**, **Kahlenberg JM**, **Gudjonsson JE.** Cytokinocytes: the diverse contribution of keratinocytes to immune responses in skin. *JCI Insight* 5: e142067, 2020. doi:10.1172/jci.insight.142067.
61. **Delitto D**, **Judge SM**, **Delitto AE**, **Nosacka RL**, **Rocha FG**, **DiVita BB**, **Gerber MH**, **George TJ Jr**, **Behrns KE**, **Hughes SJ**, **Wallet SM**, **Judge AR**, **Trevino JG.** Human pancreatic cancer xenografts recapitulate key aspects of cancer cachexia. *Oncotarget* 8: 1177–1189, 2017. doi:10.18632/oncotarget.13593.
62. **Deasy BM**, **Feduska JM**, **Payne TR**, **Li Y**, **Ambrosio F**, **Huard J.** Effect of VEGF on the regenerative capacity of muscle stem cells in dystrophic skeletal muscle. *Mol Ther* 17: 1788–1798, 2009. doi:10.1038/mt.2009.136.

63. **Arsic N**, **Zacchigna S**, **Zentilin L**, **Ramirez-Correa G**, **Pattarini L**, **Salvi A**, **Sinagra G**, **Giacca M.** Vascular endothelial growth factor stimulates skeletal muscle regeneration in Vivo. *Mol Ther* 10: 844–854, 2004. doi:10.1016/j.ymthe.2004.08.007.
64. **Song W**, **Kir S**, **Hong S**, **Hu Y**, **Wang X**, **Binari R**, **Tang HW**, **Chung V**, **Banks AS**, **Spiegelman B**, **Perrimon N.** Tumor-derived ligands trigger tumor growth and host wasting via differential MEK activation. *Dev Cell* 48: 277–286.e276, 2019. doi:10.1016/j.devcel.2018.12.003.
65. **Beltrà M**, **Pin F**, **Ballarò R**, **Costelli P**, **Penna F.** Mitochondrial dysfunction in cancer cachexia: impact on muscle health and regeneration. *Cells* 10: 3150, 2021. doi:10.3390/cells10113150.
66. **Huot JR**, **Pin F**, **Essex AL**, **Bonetto A.** MC38 tumors induce musculoskeletal defects in colorectal cancer. *Int J Mol Sci* 22: 1486, 2021. doi:10.3390/ijms22031486.
67. **Pin F**, **Prideaux M**, **Huot JR**, **Essex AL**, **Plotkin LI**, **Bonetto A**, **Bonewald LF.** Non-bone metastatic cancers promote osteocyte-induced bone destruction. *Cancer Lett* 520: 80–90, 2021. doi:10.1016/j.canlet.2021.06.030.
68. **Pin F**, **Prideaux M**, **Bonewald LF**, **Bonetto A.** Osteocytes and cancer. *Curr Osteoporos Rep* 19: 616–625, 2021. doi:10.1007/s11914-021-00712-9.
69. **Pin F**, **Bonewald LF**, **Bonetto A.** Role of myokines and osteokines in cancer cachexia. *Exp Biol Med (Maywood)* 246: 2118–2127, 2021. doi:10.1177/15353702211009213.
70. **Sindhu K**, **Jung BC**, **Glazener EM**, **Gomez M**, **Lee M**, **Lee SPH**, **Daroui P**, **Wei RL.** Bone mineral density loss in cervical vertebrae following radiation therapy for head and neck cancers. *Int J Radiat Oncol Biol Phys* 99: E373, 2017. doi:10.1016/j.ijrobp.2017.06.1491.
71. **Tsur N**, **Segal E**, **Kurman N**, **Tzelnick S**, **Wiesel O**, **Wilk L**, **Hamzany Y**, **Bachar G**, **Shoffel-Havakuk H.** Post-radiotherapy osteomyelitis of the cervical spine in head and neck cancer patients. *BJR Open* 5: 20230001, 2023. doi:10.1259/bjro.20230001.
72. **Essex AL**, **Pin F**, **Huot JR**, **Bonewald LF**, **Plotkin LI**, **Bonetto A.** Bisphosphonate treatment ameliorates chemotherapy-induced bone and muscle abnormalities in young mice. *Front Endocrinol (Lausanne)* 10: 809, 2019. doi:10.3389/fendo.2019.00809.
73. **Hunt KS**, **Alspach E.** Battle within the sexes: differences in male and female immunity and the impact on antitumor responses. *Cancer Immunol Res* 12: 17–25, 2024. doi:10.1158/2326-6066.CIR-23-0005.
74. **Lee J**, **Nicosia M**, **Hong ES**, **Silver DJ**, **Li C**, **Bayik D**, **Watson DC**, **Lauko A**, **Kay KE**, **Wang SZ**, **Johnson S**, **McGraw M**, **Grabowski MM**, **Kish DD**, **Desai AB**, **Goodman WA**, **Cameron SJ**, **Okada H**, **Valujskikh A**, **Fairchild RL**, **Ahluwalia MS**, **Lathia JD.** Sex-biased T-cell exhaustion drives differential immune responses in glioblastoma. *Cancer Discov* 13: 2090–2105, 2023. doi:10.1158/2159-8290.CD-22-0869.